

A Multi-Wavelength Analysis of Active Regions and Sunspots by Comparison of Automatic Detection Algorithms

C. Verbeeck¹ · P.A. Higgins² · T. Colak³ ·
F.T. Watson⁴ · V. Delouille¹ ·
B. Mampaey¹ · R. Qahwaji³

© Springer

Abstract Since the *Solar Dynamics Observatory* (SDO) began recording ~ 1 TB of data per day, there has been an increased need to automatically extract features and events for further analysis. Here we compare the overall detection performance, correlations between extracted properties, and usability for feature tracking of four solar feature-detection algorithms: the Solar Monitor Active Region Tracker (SMART) detects active regions in line-of-sight magnetograms; the Automated Solar Activity Prediction code (ASAP) detects sunspots and pores in white-light continuum images; the Sunspot Tracking And Recognition Algorithm (STARA) detects sunspots in white-light continuum images; the Spatial Possibilistic Clustering Algorithm (SPoCA) automatically segments solar EUV images into active regions (AR), coronal holes (CH) and quiet Sun (QS). One month of data from the SOHO/MDI and SOHO/EIT instruments during 12 May – 23 June 2003 is analysed. The overall detection performance of each algorithm is benchmarked against National Oceanic and Atmospheric Administration (NOAA) and Solar Influences Data Analysis Centre (SIDC) catalogues using various feature properties such as total sunspot area, which shows good agreement, and the number of features detected, which shows poor agreement. Principal Component Analysis indicates a clear distinction between photospheric properties, which are highly correlated to the first component and account for 52.86% of variability in the data set, and coronal properties, which are moderately correlated to both the first and second principal components. Finally, case studies of NOAA 10377 and 10365 are conducted to determine algorithm stability for tracking the evolution of individual features. We find that magnetic flux and total sunspot area are the best indicators of active-region emergence. Additionally, for NOAA 10365, it is shown that the onset of flaring occurs during both periods of magnetic-flux emergence and complexity development.

¹ Royal Observatory of Belgium, Belgium email: cis.verbeeck@oma.be

² Trinity College Dublin, Ireland email: pohuigin@gmail.com

³ University of Bradford, UK email: t.colak@bradford.ac.uk

⁴ University of Glasgow, UK email: f.watson@astro.gla.ac.uk

Keywords: Active Regions; Magnetic Fields; Coronal Structures; Sunspots

1. Introduction

In the 1960s, NASA launched the Pioneer 6, 7, 8, and 9 spacecraft, that were tasked with observing the solar wind and interplanetary magnetic fields, forming the first space-based space-weather network and recording 512 bits per second. By comparison, the recently launched *Solar Dynamics Observatory* (SDO) is currently relaying solar data back to Earth at a rate of 150 000 000 bits per second. With SDO returning the equivalent of an image with 4096 by 4096 pixels every second, human analysis of every image would require a large team of people working 24 hours a day. The technological advances that have allowed the increased flow of data, such as improving communication bandwidths and onboard processing power, allows us to record data with a much greater cadence and spatial resolution than ever before. However, there are problems with the storage, transfer, and analysis of such a large flow of data. SDO generates around 1 TB of data per day which is unprecedented in solar physics. Getting this volume of data to researchers around the world, as well as storing it in convenient places for analysis, is essential to make good use of it. An effective solution to the problem is to use automated feature-detection methods, which allow users to selectively acquire interesting portions of the full data set.

Development of automated solar feature detection and identification methods has increased dramatically in recent years due to the growing volume of data available. An overview of the fundamental image-processing techniques used in these algorithms is presented in Aschwanden (2010). These techniques are used to detect many features in various types of observations at different heights in the solar atmosphere (Pérez-Suárez *et al.*, 2011). In this present work, we focus on detecting sunspot groups and active regions in photospheric continuum images, magnetograms, and EUV images. Previously, detection of sunspot groups in photospheric images was investigated by Zharkov *et al.* (2004) and Curto, Blanca, and Martínez (2008). As well as detecting sunspot groups, Nguyen, Nguyen, and Nguyen (2005); Colak and Qahwaji (2008) also make automated classifications. The detection of active regions in magnetograms is explored in McAteer *et al.* (2005); LaBonte, Georgoulis, and Rust (2007a), Lefebvre and Rozelot (2004) and Qahwaji and Colak (2006), while Dudok de Wit (2006) introduces a supervised segmentation of EUV images into AR, CH, and QS regions.

The purpose of this article is to determine the robustness of four algorithms for detecting and physically characterising active regions and sunspot groups by comparison of their outputs. We determine overall detection performance, the correlations between extracted feature properties using Principal Component Analysis, and the usability of these algorithms for tracking feature evolution over time. The tools that we consider are the Solar Monitor Active Region Tracker (SMART: Higgins *et al.*, 2011) which detects magnetic features using magnetograms, the Automated Solar Activity Prediction code (ASAP: Colak and Qahwaji, 2009) which detects sunspots and pores using photospheric intensity images, the Sunspot Tracking And Recognition Algorithm (STARA:

Watson *et al.*, 2009) which also detects sunspots in photospheric intensity images, and the Spatial Possibilistic Clustering Algorithm (SPoCA: Barra *et al.*, 2009) which detects active regions in the corona using extreme ultraviolet images. More detail on how these algorithms operate is provided in Section 3.

The overall performance of the algorithms is compared by determining the total number of features detected as well as their full-disk area. Our methods are benchmarked against National Oceanic and Atmospheric Administration (NOAA) and Solar Influences Data Analysis Centre (SIDC) catalogues. Few studies include comparisons of detection methods or different data types. Benkhalil *et al.* (2006) compare the detection of active regions in several data types using a single region-growing method. Other studies compare the detection of features in magnetograms using a variety of region-growing and morphological methods (DeForest *et al.*, 2007; Parnell *et al.*, 2009). Direct comparison of algorithms is important for their characterisation, as each is designed in a different way to detect features for a specific purpose.

Correlations between the properties determined by the algorithms are investigated using Principal Component Analysis (Jolliffe, 2002). PCA has been used previously for various purposes in solar-physics and space-weather literature, *e.g.* to detect outliers (Sarro and Berihuete, 2011), to reduce dimensionality (Dudok de Wit and Auchère, 2007), or for exploratory data analysis of space-weather data sets (Habash Krause, Franz, and Stevenson, 2011).

Finally, the stability of the algorithms is tested for tracking feature evolution through time. The evolution of two ARs is studied in detail, including their emergence in several layers of the solar atmosphere. Lites *et al.* (1995) present a similar multi-layered analysis of the emergence of an AR. As non-potentiality increases in an AR, it may begin to exhibit enhanced coronal activity. This effect has been studied in many articles, and it is related to dynamic behaviours such as helicity injection (Morita and McIntosh, 2005), turbulent cascades (Hewett *et al.*, 2008; Conlon *et al.*, 2008, 2010), enhanced polarity separation line gradient (Falconer, Moore, and Gary, 2008), and changes in magnetic connectivity (Georgoulis and Rust, 2007; Ahmed *et al.*, 2010). In this article we study multiple behaviours in the same AR using magnetic property determinations. Finally, the decay of the AR in the corona and photosphere is compared. To our knowledge, this is the first time that automated feature-detection algorithms have been used to study temporal evolution using properties of magnetic non-potentiality, sunspot characteristics, and coronal activity of ARs simultaneously.

The following sections detail these investigations. Observations used in this study are described in Section 2, and the four algorithms to be compared are introduced in Section 3. Our results are presented in Section 4, including an evaluation of the algorithms' overall performance, a correlation study of the complete sample of active regions and a detailed case study of two different active regions. Finally, a discussion of the results and concluding remarks is presented in Section 5.

2. Observations

In this study we analyse data from the interval 12 May–23 June 2003. The detections obtained from each algorithm for the entire data set are studied as a whole in Section 4.2 and NOAA ARs 10377 and 10365 are individually studied in detail in Section 4.3. This particular data set was selected for the diversity of solar features present. SOHO/MDI magnetograms are used for magnetic region detection by SMART, while SOHO/MDI continuum images are used for sunspot detection by ASAP and STARA, and SOHO/EIT images are employed for active region detection by SPoCA. These algorithms are described in Section 3.

The MDI instrument on SOHO provides almost continuous observations of the Sun in the white-light continuum, in the vicinity of the Ni I 676.78 nm photospheric absorption line. These photospheric intensity images are primarily used for sunspot observations. MDI data are available in several processed “levels”. We used level-2 images, which are smoothed, filtered, and rotated (Scherrer *et al.*, 1995). SOHO provides two to four MDI photospheric intensity images per day with continuous coverage since 1995.

Using the same instrument level, 1.8 line-of-sight (LOS) MDI magnetograms are recorded with a nominal cadence of 96 minutes. The magnetograms show the magnetic fields of the solar photosphere, with negative (represented as black) and positive (as white) areas indicating opposite LOS magnetic-field orientations.

The *Extreme Ultraviolet Telescope* (EIT: Delaboudinière *et al.*, 1995), on-board SOHO, delivers synoptic observations consisting of 1024 by 1024 images of the solar corona recorded in four different wavelengths every six hours. Every SPoCA segmentation in this article was based on a pair of 17.1 and 19.5 nm EIT images. All images used have been preprocessed using the standard eit-prep procedure of the SolarSoftware library. A fixed-centre segmentation with six classes was performed on the logarithms of the image pixel values. The AR centre values are 401.74 and 324.25 DN s⁻¹ in 17.1 and 19.5 nm, respectively. These values were derived from a cumulative run of SPoCA on a data set of monthly EIT image pairs from February 1997 until April 2005; see Barra *et al.* (2009).

In the case studies presented in Section 4.3, we compare observations of NOAA 10365 and 10377 with flares characterised by the *Reuven Ramaty High Energy Solar Spectroscopic Imager* (RHESSI) team and distributed in the RHESSI flare list.

3. Methods

SMART, ASAP, and STARA detect photospheric features such as active regions and sunspots while SPoCA uses images in the extreme ultraviolet to observe active regions at the coronal level. In this section, we will describe each of the feature-detection algorithms used (Sections 3.1, 3.2, 3.3, and 3.4). The outputs from each of the algorithms are associated using the method explained in Section 3.5.

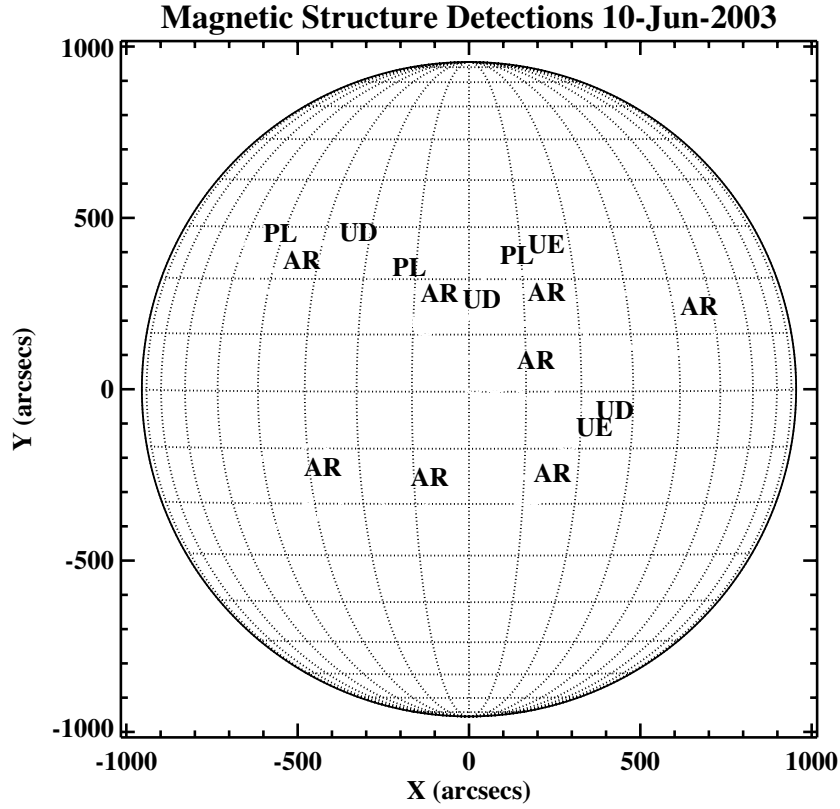


Figure 1. An example set of SMART detections from 10 June 2003. PL, UD, and UE identify three classes of unipolar feature, while AR denotes multipolar features.

3.1. The SMART algorithm

The Solar Monitor Active Region Tracker (SMART: Higgins *et al.*, 2011) is an algorithm that uses magnetograms to automatically extract, characterise, and track active regions over multiple solar rotations – from first emergence to decay. This allows one to study the complete life-cycle of ARs. The algorithm uses a combination of image-processing techniques to determine the boundary of an AR. Two consecutive line-of-sight magnetograms are smoothed using a gaussian kernel with a full-width at half-maximum of five pixels and thresholded by 70 G to identify potential features. The two detections are overlaid to identify and remove features that are not present in both magnetograms. The remaining detection boundaries are then dilated by ten pixels to create the final mask.

Dilation is performed to include nearby decaying and plage fragments that may have separated from the main AR. This is intended to help conserve the measured polarity balance of the AR as it evolves. An example set of SMART detections is shown in Figure 1. In this article, SOHO/MDI LOS magnetograms are used for detection, but recently the algorithm has been adapted for use with SDO/HMI magnetograms (For near-realtime detections, see http://solarmonitor.org/smart_disk). ■

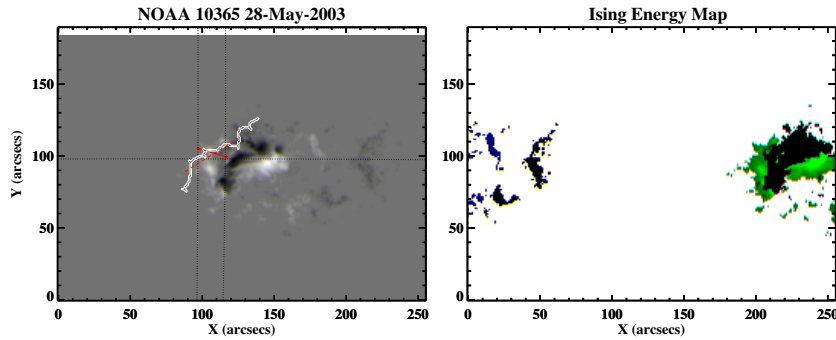


Figure 2. Left: NOAA 10365 highlighting the PSL (white contour), a linear fit to the locus of PSL positions (dotted red line), bipolar connection line (solid red line), and heliographic longitude and latitude reference lines (dotted black lines). Right: An Ising energy map of the same region. Red represents the magnitude of energy for each pixel from highest (light) to lowest (dark). Since the connection between pixels of opposite polarity is being represented, the energy map is only shown for one of the polarities.

Several new physical-property modules have been added to SMART for this study. The tilt of an AR is obtained by measuring the angle between the line connecting the centroids of the largest flux-weighted positive and negative blobs (solid red line in left panel of Figure 2) and the heliographic-latitude line passing through the centroid of the AR. The length of this bipolar connecting line [BCL] line is also determined and provides a measure of the relative compactness of an AR when compared to the evolution of AR area (left panel of Figure 2). Additionally, the angle $[\alpha]$ detected between the best-fit line to the locus of pixels forming the main polarity separation line [PSL] and the BCL is measured. The main PSL is defined as the interface between the aforementioned largest flux-weighted positive and negative blobs. The temporal derivative of the angle α is shown to be a useful proxy for the occurrence of helicity injection in an AR (Morita and McIntosh, 2005), which may be an important flare predictor (LaBonte, Georgoulis, and Rust, 2007b). The evolution of this angle is studied in Section 4.3. These properties are less informative when studying AR complexes or non-bipolar ARs, since often no main axes can be discerned, making a description of the AR orientation impossible.

The original Ising model is used for the analysis of magnetic interactions and structures of ferromagnetic substances. Here, as by Ahmed *et al.* (2010), Ising energy is used as a proxy for magnetic connectivity and complexity within an AR (right panel of Figure 2). We use a modified form of that given by Ahmed *et al.* (2010).

This version is calculated using

$$\sum_{i,j} \left| \frac{B_i B_j}{D_{ij}} \right|, \quad (1)$$

where B_i (B_j) are pixel values of positive (negative) line-of-sight magnetic field and D_{ij} is the spatial distance between pixels i and j . The Ising energy increases



Figure 3. An example set of ASAP detections from 10 June 2003.

as the negative and positive magnetic footprints within an active region become more entangled. The evolution of this property is studied in Section 4.3.

The modules added to **SMART** for this work will be used for future large-scale active region studies and will be added to the pipe-line versions of **SMART** running at the Heliophysics Events Knowledgebase (<http://www.lmsal.com/hek/index.html>; Hurlburt *et al.*, 2010) and included in the Heliophysics Integrated Observatory (<http://www.helio-vo.eu/index.php>; Bentley *et al.*, 2009). In the future, other property modules will be added to calculate a physically motivated magnetic-connectivity measurement (Georgoulis and Rust, 2007), multi-scale energy spectrum slope (Hewett *et al.*, 2008), and multi-fractal spectrum properties (Conlon *et al.*, 2008).

3.2. The ASAP algorithm

Automated Solar Activity Prediction (**ASAP**) is the collective name for a set of algorithms used to process solar images. It is composed of algorithms for sunspot, faculae, and active-region detections (Colak and Qahwaji, 2008) and solar-flare prediction (Colak and Qahwaji, 2009). Unlike other algorithms described in this article, **ASAP** uses quick look (in GIF or JPEG format) images for its processes. In this article a recently developed sunspot detection algorithm for **ASAP** is used. This new sunspot-detection algorithm works with continuum images and is described in detail by Colak *et al.* (2011). The main steps in this algorithm can be summarized as follows:

-
- Images are pre-processed to detect the solar disk, and to remove limb darkening.
 - Detected solar-disk data are converted from heliocentric coordinates to Carrington heliographic coordinates.
 - The key point in heliographic conversion is to choose the size of the resulting image. If a very small image size is selected, this will cause truncation and loss of data. If a very large one is chosen, there will be many spaces in the resulting image. In this study, each heliographic degree is represented by ten pixels therefore the resulting heliographic images are 3600 by 1800 pixels.
 - Initially, an empty 3600 by 1800 image is created. When the Carrington longitude and latitude of all of the pixels on the solar disk are calculated, their pixel intensities are placed in corresponding locations.
 - The distribution of pixels representing degrees in heliocentric coordinates is not uniform due to the spherical shape of the Sun. Towards the limb of the Sun on a two dimensional heliocentric image each degree will be represented by fewer pixels although in a heliographic image each degree is represented with same amount of pixels. Size of the heliographic image is larger than heliocentric image and therefore there will be gaps (empty pixels that are not filled with data from heliocentric image) in the resulting initial heliographic image after conversion.
 - The following algorithm is applied to estimate the pixel intensities of the gaps in the heliographic image. Every pixel on the heliographic image is examined and when a pixel without any information is found, its neighbouring pixels are searched using variable-size windows. First a 3×3 pixel window is centred on the empty pixel and the values of the non-empty neighbouring pixels within this window are added. If all the neighbouring pixels within the initial window were empty, the size of the window is increased by one and the process continued until at least one pixel with information is available within the window. Then the average value of the valid pixels found within the final window is assigned to the empty pixel. The algorithm continues until all of the pixels have been processed.
 - After all data gaps have been filled, a smoothing algorithm using a 3×3 linear uniform filter is applied to create the final heliographic image.
 - Subsequently, the following filter is applied to the Carrington heliographic image for detecting sunspots:
 - An intensity filtering threshold value $T = \mu - (\sigma \times \alpha)$ is calculated where μ is the mean, σ is the standard deviation of the image, and α is a constant equal to 2.5.
 - The intensity of each pixel in the image is compared to this T value. If it is less than the calculated threshold value, the pixel under consideration is marked as a sunspot.

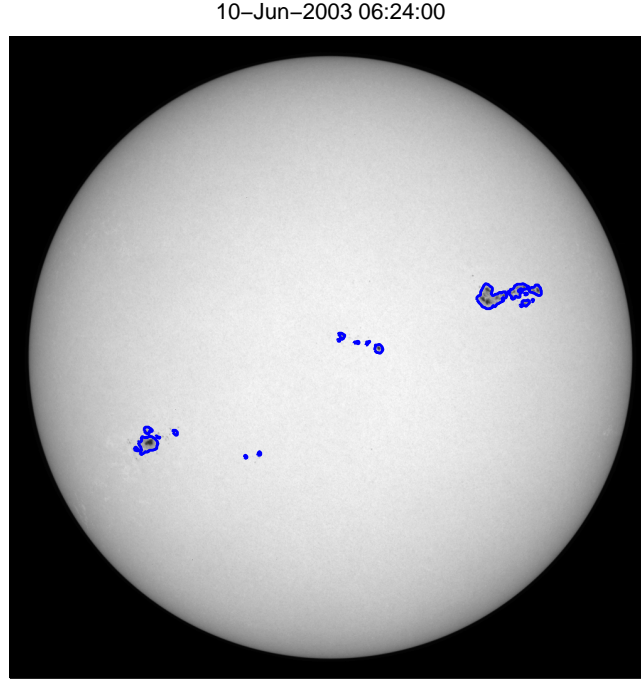


Figure 4. An example set of STARA detections from 10 June 2003.

Although heliographic conversion can be computationally expensive, it yields detections that are more accurate compared to the ones done on heliocentric coordinates. A tracking algorithm was added to ASAP for this study, finding the intersections between objects (*e.g.* sunspots) on two consecutive heliographic images. Since the differential rotation is very small in Carrington heliographic coordinates, there is no need for longitudinal corrections. ASAP tends to detect small sunspots, which can be classified as pores. This is useful especially when grouping and classifying sunspots. However, the number of tracked sunspots increases because most pores are only visible for a few hours on the solar disk. An example set of ASAP detections is shown in Figure 3.

It was not necessary to update ASAP for this work, but some computational issues have been discovered. For instance, the application of ASAP to SDO/HMI images larger than 1024×1024 pixels shows that heliographic conversion algorithms must be made more efficient to tackle larger images.

3.3. The STARA algorithm

The Sunspot Tracking And Recognition Algorithm (STARA) code was written in 2008 in order to perform consistent long term observations of sunspots over Solar Cycle 23 (Watson *et al.*, 2009). It was originally developed for use with

MDI data but has since been extended for use with data from SDO as well as from a number of ground-based instruments. A simple detection method was required to speed up processing when large data sets were used and suitable techniques were found in the field of morphological image processing.

The STARA detection method works as follows: The image is read in and inverted so that the sunspots appear as bright areas on a dark background for compatibility with the top-hat transform. Morphological erosion is applied, which removes peaks and works by treating the 2D image as a 3D surface with the pixel values indicating the height of the surface at that point. A probe known as a structuring element is then chosen (in this case, a sphere with a radius of 14 MDI pixels) and is “rolled” underneath the surface whilst always touching it. The centre of the sphere then maps out a new surface that is close to 14 units below the original. However, any sharp peaks present (such as sunspots) would not allow the sphere to fit inside them and so are not represented in the eroded image. A morphological dilation is then performed which is identical to an erosion apart from the sphere being rolled on top of the surface. The dilated surface is subtracted from the original to leave only the sunspot peaks present.

As the sphere rolls over the surface it also carries the limb-darkening profile through each step and when the final surface is subtracted from the original, the limb-darkening effects are automatically removed.

More detail on this step and the top-hat transform is given by Watson *et al.* (2009) and Dougherty and Lotufo (2003). A size filter is then applied that removes areas containing less than ten pixels as they are far more likely to be pores than sunspots. The remaining areas are recorded along with their locations as well as the number of umbral regions detected within the sunspot boundary. This is repeated for a number of consecutive images and using the solar-rotation model of Howard, Harvey, and Forgach (1990) the sunspots can be tracked throughout a sequential data set. This allows the evolution of individual sunspots to be followed as well as the overall properties of the sunspot population as a whole. An example of a typical set of STARA sunspot detections is given in Figure 4.

STARA has undergone very few changes over the course of this work as the code was well established beforehand. Nevertheless, some subtle problems have been discovered in the process. As sunspots approach the limb (at longitudes greater than 75°) the sunspot position returned by the code quickly loses accuracy. This is a common problem with feature-detection methods as the geometrical foreshortening effects test the limits of automated systems. There are also potential problems present with bad data. Obviously the best remedy is to remove it altogether but with MDI it is possible to have images with only half of the solar disk present or with large artifacts. Both of these situations can have substantial effects on the detected global properties and cause problems with analysis.

3.4. The SPoCA algorithm

The Spatial Possibilistic Clustering Algorithm (SPoCA) is a multi-channel fuzzy clustering algorithm that automatically segments solar EUV images into a set of features; see Barra *et al.* (2009) for a complete presentation. It optimally separates active regions, quiet Sun, and coronal holes, even though the boundaries

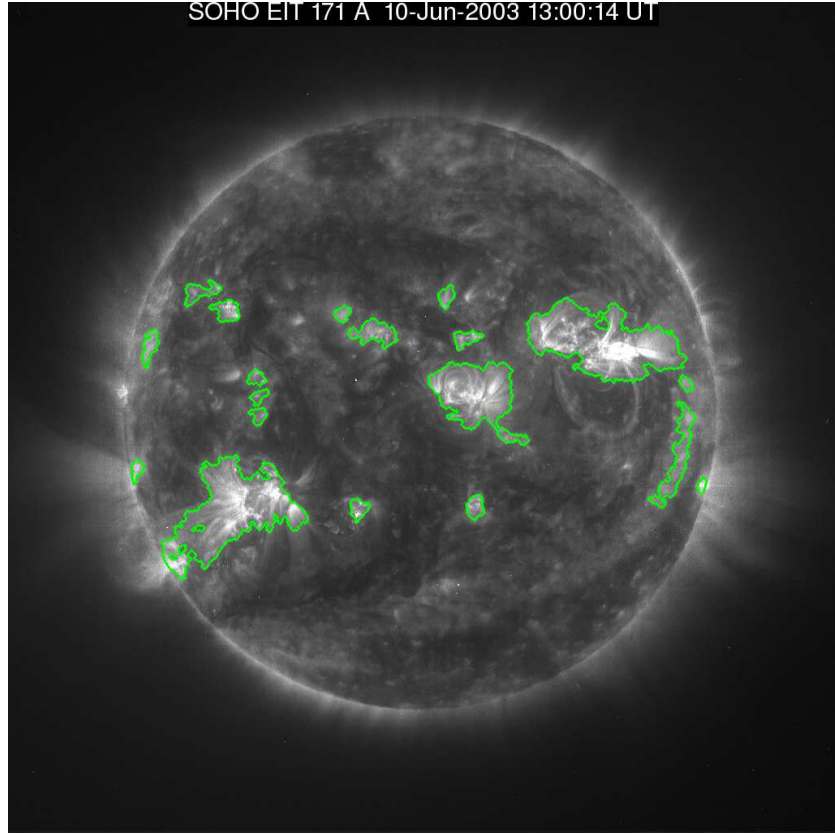


Figure 5. An example set of SPoCA detections from 10 June 2003.

of these regions are not always well defined. The description of the segmentation process in terms of fuzzy logic was motivated by the facts that information provided by a solar EUV image is noisy (corruption by Poisson and readout noise as well as by cosmic-ray hits) and subject to both observational biases (line-of-sight integration of a transparent volume) and interpretation (the apparent boundary between regions is a matter of convention).

SPoCA takes as input an image in one (or several) EUV passband(s) and uses as “feature vector” the pixel value (or the pixel value vector in the multi-channel case) in order to classify a pixel as belonging to one of three classes, namely AR, QS, and CH. SPoCA is based on a fuzzy clustering technique called “Possibilistic C-Means” (PCM: Krishnapuram and Keller, 1993, 1996). For each class, it assigns a “probability” or membership value $\in [0, 1]$ to every feature vector.

PCM is an iterative method that searches for three compact clusters in the space of feature vectors, corresponding to AR, QS and CH. In practice, this is achieved through a gradient-descent scheme that minimizes an objective function that is related to the total intracluster variance plus some penalty term. In every iteration, new membership values are calculated based on the class centre values.

The membership values are used in turn to compute the new class centres, and so on, until the class centres converge to within a preset accuracy.

In order to cope successfully with intensity outlier pixels such as those affected by cosmic rays and proton storms, a spatial regularization term was added to the PCM objective function, forcing membership values in a neighbourhood to be as close as possible. By assigning each pixel to the class for which its feature vector has the largest membership value, the image is segmented. An example set of SPoCA detections is shown in Figure 5.

Since the solar corona is optically thin, and since the intensity in EUV images is obtained through an integration along the line of sight, there is a limb-brightening effect in those images, which may hinder the segmentation process. Therefore, the EUV images are pre-processed so as to lower the enhanced brightness near the limb. The initial SPoCA class contours are automatically postprocessed using a morphological opening with a circular isotropic element of size unity.

Since the publication of Barra *et al.* (2009), the SPoCA algorithm was optimized and extended in several ways:

- In order to gain more consistent results, we introduced some constraints on the penalty term of the objective function to be minimized.
- The limb correction is now applied in a continuously increasing way towards the limb instead of introducing it abruptly from some point onwards.
- For individual AR detection, first the Bright Points are removed (size threshold is 1500 square arcseconds) and then a spherical dilation (radius: 12 EIT pixels) is employed to group the remaining bright blobs into individual active regions.
- Individual AR are tracked through time by comparing the masks of regions in two consecutive time frames, taking into account differential rotation.

SPoCA has been running in near-realtime on AIA data since September 2010 as part of the SDO Feature Finding Project (Martens *et al.*, 2011), a suite of software pipeline modules for automated feature recognition and analysis for the imagery from SDO. The resulting AR events are automatically ingested by the Heliophysics Events Knowledgebase (Hurlburt *et al.*, 2010).

SPoCA is the only algorithm presented here that detects ARs in the solar corona. The method is generic enough to allow the introduction of other channels or data. It has been applied to SOHO/EIT, SDO/AIA, PROBA2/SWAP, and STEREO/EUVI images, and could potentially be used on other multi-channel maps such as Differential Emission maps. In this article we focus on ARs, but QS and CH can also be detected and tracked.

3.5. Association of Detected Features

The SMART tracking module, called “Multiple Disk Passage” (MuDPie: Higgins *et al.*, 2011), is used to associate individual SMART detections of the same physical feature over time by comparing the centroids of all detections in consecutive magnetograms. Two detections are associated if their centroids match within 5° heliographic latitude and longitude. The tracked SMART detections are then

associated with the best matched detections in each of the other algorithms as described in the following paragraphs.

In order to analyse the relation between the features detected by different algorithms, a routine developed in Python associates detections from each algorithm in two ways. First outputs from ASAP, STARA, and SPoCA are associated with SMART outputs based on time and location information. Second, individual association outputs (ASAP *vs.* SMART, STARA *vs.* SMART, SPoCA *vs.* SMART) from the first step are combined using SMART IDs and timing information.

For associations, SMART is chosen as the base algorithm because SMART detections usually encircle the corresponding ASAP and STARA detections and they are also more stable over time than SPoCA detections, due to the frequent splitting and merging of coronal AR detected by SPoCA. Also, SMART detects magnetic regions from MDI images which are more frequently available than the continuum and EIT images that the other algorithms are working on. The association rules are described below.

First Step: Individual associations (ASAP, STARA, SPoCA *vs.* SMART)

- The time difference between the solar detections under consideration (*i.e.*, sunspots from ASAP and STARA, active regions from SPoCA *versus* magnetic regions from SMART) is calculated.
- If the time difference between a magnetic region detected by SMART and a solar region detected by another algorithm is less than 0.2 Julian days and their heliographic bounding boxes intersect, then these detections are associated. Since SPoCA does not deliver heliographic bounding boxes, a bounding box of 5° in longitude and latitude is assumed.
- If the same solar detection is associated to more than one SMART region, only the closest (in terms of time and distance between centres) SMART region is selected as associated.
- Associations are saved in separate files (three files; ASAP *vs.* SMART, STARA *vs.* SMART, SPoCA *vs.* SMART) including the selected characteristics from each algorithm.
output that is going to be analysed.

Second Step: Combining all of the associations

- The SMART algorithm uses an ID for each magnetic region detected and in this second step, the association data saved in the three separate files from the first step are combined using this ID and time information. The association data with same SMART ID and closest timing are combined together. Timing information still has to be used due to the difference between the image times.
- The final combined data are saved in one file.

SMART provided 9356 detections (207 magnetic region features), ASAP 3039 detections (952 sunspot features), STARA 1329 detections (433 sunspot features) and SPoCA 1222 detections (190 coronal active-region features) within the considered time-frame. In the first step, 714 SMART detections were associated to

2889 ASAP detections, 550 SMART detections were associated to 1315 STARA detections and 1089 SMART detections were associated to 1117 SPoCA detections. In the second step when all of these data were combined, 350 detection (33 feature) associations were created for SMART, ASAP, STARA and SPoCA. The daily averages of some of the outputs such as average daily sunspot numbers, active region numbers and average areas are compared to the NOAA active region catalogue in Section 4.1. In the considered period, NOAA recorded 217 detections (37 features).

In case of merging or splitting of neighbouring coronal regions as detected by SPoCA, the association procedure described above does not relate the new SPoCA detection to the corresponding SMART detection. This happened several times in the case studies in Section 4.3. For these cases, we applied a manual association of SPoCA detections to SMART detections.

4. Results

The feature detections from each algorithm are compared in the following sections. First, in Section 4.1 the overall detection performance of the algorithms is presented, and compared to the corresponding NOAA detections and the daily international sunspot number. Next, Principal Component Analysis is performed on the full set of detections to probe the overall structure of the physical properties calculated by the algorithms in Section 4.2. Finally, in Section 4.3 the evolution and flare activity of NOAA 10377 and 10365 are analysed in depth, using physical properties determined by each algorithm.

4.1. Algorithm Performance

The performance of the algorithms is measured by comparing the daily total and average values of some of the solar feature properties to each other, to values reported by NOAA (<http://www.swpc.noaa.gov/ftpdir/forecasts/SRS/README>), and to the international daily sunspot numbers (SIDC-Team, 2003) between 12 May and 23 June 2003.

A comparison of these data is provided in Figure 6. The graph on the upper left side of Figure 6 compares the daily number of sunspots detected by ASAP and STARA to the total number of spots within NOAA regions and to the international sunspot number. Generally, peaks and valleys in all of the series follow each other but the international sunspot numbers and the sunspot numbers for NOAA are usually higher than the sunspot numbers for ASAP and STARA. When sunspots are detected manually, each umbra within a penumbra is counted as one sunspot, whereas the automated algorithms discussed here count each penumbra as one sunspot although it could have more than one umbra within. Therefore the difference in sunspot numbers increases when the number of complex sunspot regions increases. Also, the number of sunspots detected by ASAP is always higher than the ones detected by STARA. This is because ASAP tends to detect very small sunspots (sometimes pores) while STARA has a higher threshold for the size of sunspot candidates.

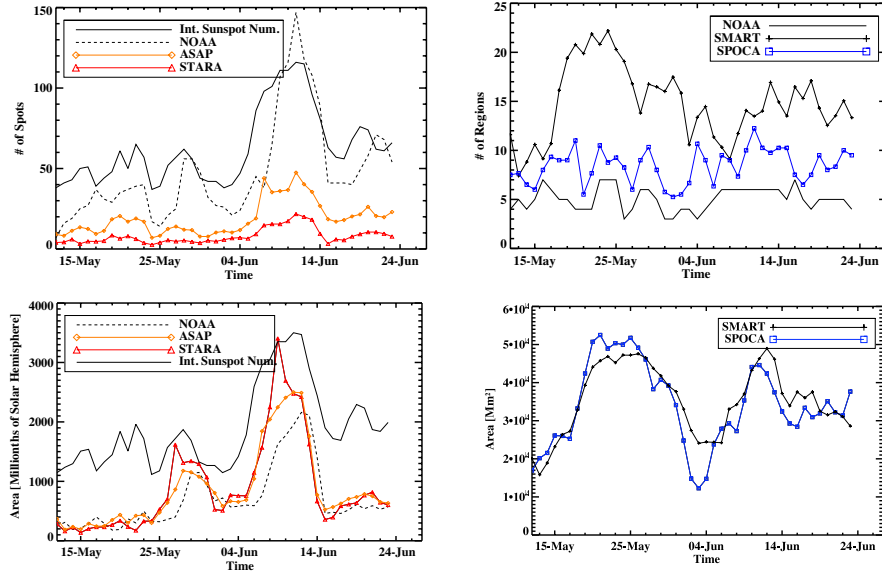


Figure 6. Comparison of average detection results of algorithms to reported NOAA and international sunspot numbers. Upper-left: Comparison of number of sunspots detected by ASAP and STARA and reported by NOAA and recorded international sunspot numbers. Upper-right: Number of regions detected by SMART and SPoCA compared with the ones reported by NOAA. Lower-left: Comparison of average daily sunspot areas detected by ASAP and STARA *versus* NOAA. The normalised international sunspot number is over-plotted for context. Lower-right: Comparison of average daily region areas detected by SMART and SPoCA.

The graph on the upper right side of Figure 6 compares the daily number of regions detected by SMART and SPoCA to the daily number of NOAA regions. SMART and SPoCA detect more regions than NOAA because the NOAA number is given to a region only if it has one or more sunspots, while SMART and SPoCA regions do not depend on the existence of sunspots within detected boundaries. Because of the projection effects of large coronal loops, two close but distinct regions in the photosphere will often be detected by SPoCA as one region. This explains why SMART has a higher tally of daily regions than SPoCA. This effect is most visible near the solar limb.

A comparison of the areas of ARs and sunspots as detected by the four algorithms and NOAA is presented in the lower part of Figure 6. SMART, ASAP, and STARA areas were corrected for the line-of-sight projection effect that decreases the observed area as the feature moves away from the central meridian. Since the line-of-sight projected area of coronal loops does not necessarily decrease with longitude, no systematic effect is expected for the observed SPoCA area, so the raw area is presented. Sunspot areas are given in millionths of solar hemisphere to be consistent with the units of the NOAA catalogue.

The graph on the lower left side of Figure 6 compares the sunspot areas detected daily by ASAP and STARA to the NOAA sunspot areas, while the international sunspot number is added for context. These three time series agree well but there appears to be a one-day shift in NOAA sunspot areas. The ASAP and STARA sunspot measurements are averages of observations throughout the

whole day, whereas, depending on the day, the NOAA sunspot observation may be quite early in the day. Since sunspots emerge quickly and decay slowly, any sunspots that emerge late in a day are likely to be missed by NOAA, but registered by ASAP and STARA. The following day, the new sunspots are likely to remain visible, so ASAP and STARA are likely to show the same area as the previous day, while the NOAA area will increase.

The graph on the lower right side of Figure 6 shows the comparison between active region areas detected daily by SMART and by SPoCA. Considering we are dealing here with photospheric *versus* coronal areas, a good agreement between the areas is obtained. Both SMART and SPoCA areas vary smoothly. Moreover, they are large enough to include the whole sunspot group if present, and to measure changes in topology or complexity consistently. In summary, the time series of sunspot and AR areas are well correlated, showing similar behaviour in time, and the differences observed are likely due to the data and detection methods used.

4.2. Principal Component Analysis

Principal Component Analysis (PCA: Jolliffe, 2002) aims at reducing the dimensionality of a problem. It does so by maximizing the data structure information in the principal component space. More precisely for a data set containing n observations of p variables, the principal components are the directions in n -dimensional variable space in which the data set exhibits maximal variance.

In this article, PCA (based on linear values) is used to get some insight in the correlation structure of the following p variables: the Schrijver R value (Schrijver, 2007), length of the strong gradient line, magnetic flux, maximum B field, area, length of the bipole connecting line, Ising energy, and Ising energy per pixel (Ising E ppx) as computed by the SMART algorithm, the sunspot area and number of sunspots as given by ASAP, and the raw AR area, maximum, variance, kurtosis and skewness of the EUV intensity as computed by SPoCA.

These variables were computed on data recorded 12 May–23 June 2003, at a cadence of 96 minutes for photospheric features, and of six hours for coronal features. Data from the various algorithms were then associated as described in Section 3.5.

We excluded data points corresponding to regions whose centre was more than 60° from the central meridian, as projection errors involved become too large. Table 1 lists the percentage and cumulative percentage of the variance explained by the principal components. The first two components explain 67% of the total variability in the data set.

Figure 7 represents the variables in the plane of the first two components. Each variable lies within a circle of radius one in this figure. Variables that lie close to the circle are well represented by the first two components, while variables close to the origin are not. The cosine of the angle formed by the origin and two points on the graph of Figure 7 gives the correlation between the two corresponding variables. This figure thus yields a graphical representation of the correlation structure between variables.

Table 1. Percentage and cumulative percentage of the variance of the 15-dimensional variable space described above, that can be explained by the consecutive principal components. Note that the first two principal components comprise 67% of the variance.

Component	% variance	Cumulative % variance
1	52.86	52.86
2	14.61	67.47
3	10.30	77.77
4	6.55	84.32
5	5.17	89.49
6	3.61	93.11
7	2.82	95.93
8	1.61	97.54
9	0.93	98.47
10	0.44	98.92
11	0.39	99.30
12	0.29	99.59
13	0.22	99.81
14	0.12	99.93
15	0.07	100.00

The first observation is that no variable is strongly anti-correlated with another in this data set. Roughly speaking, all variables evolve in the same direction. A more detailed inspection shows that the Schrijver R value, the length of the strong gradient line [Lsg], and the Ising energy per pixel are strongly (positively) correlated to each other, as are the Ising Energy and the ASAP area. To a lesser extent, these five variables are all correlated to each other, as well as to the magnetic flux. This related behaviour of PSL length, R value, Ising energy, and ASAP area is apparent in Figures 9, 11, 13, 15, 16 and 18. These variables are linked to a measure of complexity of the AR and its capability to produce a flare, see Colak *et al.* (2010).

The maximum and skewness of the EUV intensity are strongly correlated: indeed a high value of maximum EUV intensity implies a long tail in the intensity distribution function, hence a high skewness. Similarly, the variance and kurtosis of the EUV intensity are strongly correlated, which is expected since they are related by definition. Note that variance and kurtosis lie further from the circle than maximum and skewness, and hence are less well represented by the first two principal components. Finally, the maximum magnetic field, length of the Bipole Connecting Line, SPoCA area, SMART area, and ASAP number of sunspots are not well represented by the two first components, and hence their correlation structure cannot be interpreted from this plot.

PCA also tends to separate photospheric and coronal contribution. Features computed at the photospheric level such as R , Lsg, Ising energy, ASAP area, and flux have a large contribution to the first component, which accounts for 52.86% of the variability in the total data set. The maximum, variance, skewness, and kurtosis in EUV intensity images are moderately correlated to both the first and second principal components.

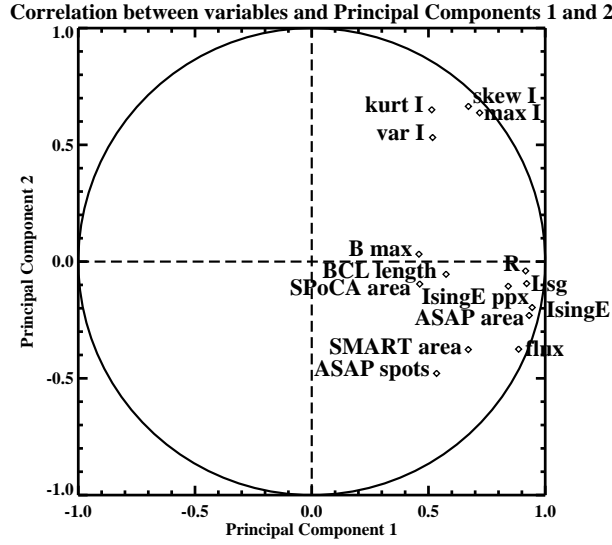


Figure 7. The projections of the algorithm variables upon the first and second principal components are plotted. They provide a measure of the extent to which these variables are correlated with the first and second principal components.

This study shows that a reduction in dimensionality using PCA can be performed without losing too much information. Such reduction can enhance the accuracy and robustness of a subsequent classification scheme (Jiang, 2011) that would aim for example at separating active regions that are prone to flares from quiet active regions.

4.3. Case Studies

In the following section we analyse the time evolution of the ARs that emerge as NOAA 10377 (a simple region) and 10365 (a complex, flaring region). Of special interest is how activity in the corona results from changes in the photosphere. Drawing this connection is essential for flare prediction, since the photosphere is more easily physically characterised than the corona, where flares actually occur. The photosphere–corona connection is not well understood, *e.g.* the work of Leka and Barnes (2007) and of Handy and Schrijver (2001), with the references therein.

We compare observations of NOAA 10365 and 10377 with flares characterised by the *Reuven Ramaty High Energy Solar Spectroscopic Imager* (RHESSI) team and distributed in the RHESSI flare list (http://sprg.ssl.berkeley.edu/~jimm/hessi/hsi_flare_list.html). The flares, which have been associated with the individual ARs by the RHESSI team, are represented in plots (Section 4.3) as downward pointing arrows, whose size is logarithmically proportional to their peak count rate.

4.3.1. NOAA 10377

NOAA 10377 first emerges just before rotating onto the visible disk on 4 June 2003. It continues to gradually develop as it progresses across the disk producing

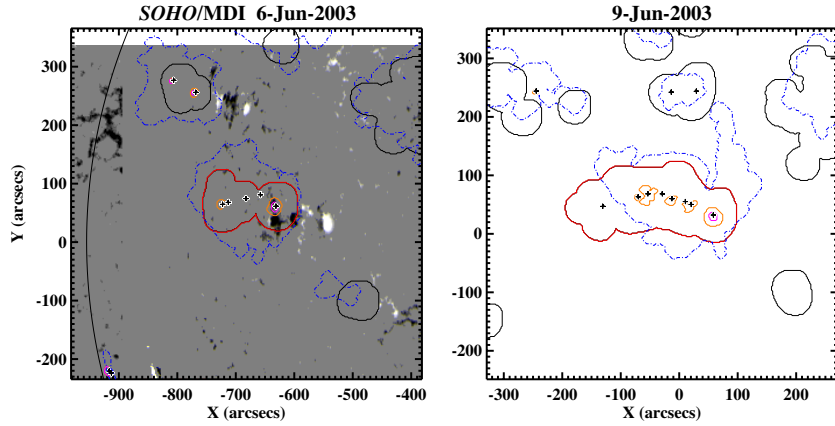


Figure 8. A comparison of NOAA AR 10377 detections. ASAP sunspots are represented by black crosses. The contours represent SMART in black (with NOAA 10377 outlined in red) for the magnetic features, SPoCA in dashed blue for coronal features, and STARA in orange for sunspot penumbrae and magenta for umbrae.

very little activity (only one B9.1 event is listed in the NOAA events catalogue (<http://www.swpc.noaa.gov/ftpdir/indices/events/README>)). Some of the flares produced by 10377 may have been missed due to the presence of 10375, which produced many large flares, swamping any signal that could be attributed to 10377.

Figure 8 shows the SMART detection of 10377 in red, while other features are outlined in black. The extended dashed blue contours are SPoCA AR detections and the small symbols and contours are sunspot detections from ASAP and STARA, respectively. It is clear from Figure 8 that positions of the SMART, ASAP, STARA, and SPoCA detections agree quite well. Whereas the sunspots detected by ASAP and STARA are well confined within the SMART magnetic region boundary, the SPoCA region most often contains most of the SMART detection. In the case of coronal loop structures forming between nearby ARs, adjacent SPoCA detections will merge and the SMART and SPoCA centroids will diverge. This is especially apparent near the solar limb, where coronal structures extending above the solar surface will be superimposed.

Figures 9–11 show the evolution of NOAA 10377 as it progresses across the disk. In the top panel of Figure 9 the Stonyhurst longitudes of the region centroids from each algorithm are shown. The vertical dotted lines indicate where the AR magnetic bounding box edges (dashed–dotted) and centroid (dashed) cross -60° and 60° longitude. The cosine correction used to correct for line-of-sight effects on magnetic-field properties is not sufficient outside of this range. Also, beyond 60° , sunspot visibility is below $\approx \frac{1}{3}$ of that at disk centre (Watson *et al.*, 2009) due to the Wilson depression.

The top panel of Figure 9 tracks the longitude of centroids over time. We see that ASAP and STARA curves are above the SMART curve on this plot, suggesting that the centroid of the magnetic footpoints (SMART) follows behind the sunspot centroids (ASAP and STARA). Since the longitudinal speed of the white-light and magnetic detections are the same, this implies that the following

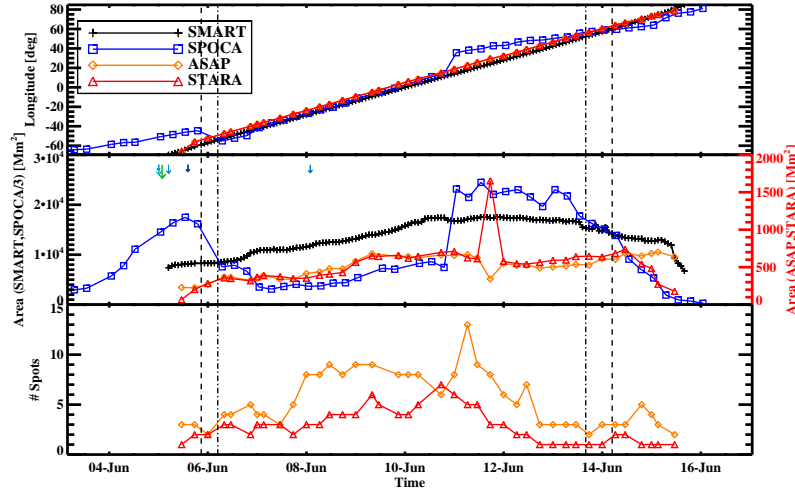


Figure 9. Time series of position, area, and sunspot information characterising the evolution of NOAA AR 10377. The legend indicates symbols and colors for each of the detection algorithms. The axes of the area plot are split between left (SPoCA and SMART) and right (ASAP and STARA). The SPoCA areas have been divided by three for display.

polarity of the AR extends beyond the embedded sunspots, while the leading polarity remains compact. As the NOAA region 10377 is close to 10375, this last region affects the SPoCA detections. From 3–6 June, SPoCA detects both NOAA regions within a single boundary. When this region splits into two parts on 6 June, the SPoCA longitude and area curves decrease abruptly, and can now be directly compared to the photospheric structures. This changes when the two NOAA regions merge again on 11 June. Whenever the region detected by SPoCA corresponds to the region detected by the other algorithms, all four longitudes agree well.

The total sunspot area determined by ASAP and STARA (Figure 9, middle) is very similar except for one data point near 12 June 2003. This is due to the MDI image on 11 June 2003 at 1736 UT being distorted. Most of the distortion is visible on the south limb of the image where this area is darker than the rest of the solar disk. Because ASAP detects the solar disk directly from the image, while STARA uses FITS keywords, the determination of the solar disk by these two methods is different. This explains why on this image the ASAP sunspot area is much smaller than the STARA area: whereas the distorted area is detected by STARA as a large sunspot, it is completely discarded by ASAP. The SMART and SPoCA areas of photospheric magnetic regions and coronal active regions obey the same general trend as the sunspot areas, although the absolute scales are different. While the area measurements are stable, the total number of sunspots is not. The total area is dominated by the largest sunspots, while the total number of spots is affected by small transients which ASAP is especially sensitive to.

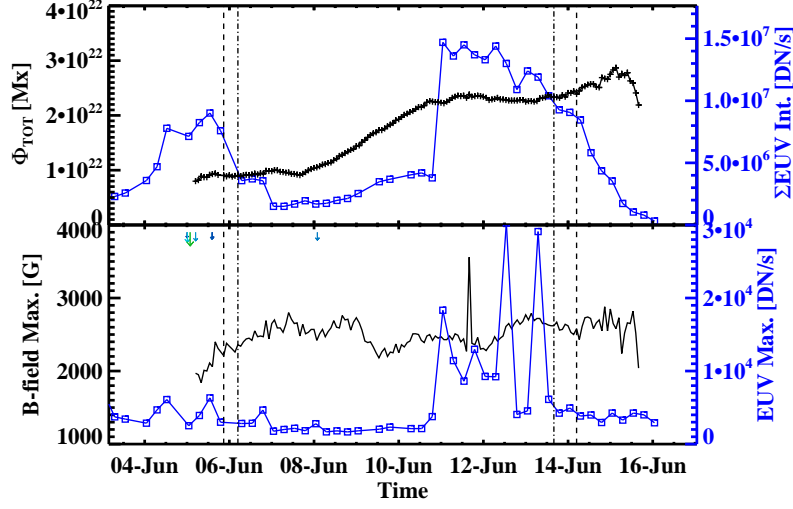


Figure 10. Time series of (top) total magnetic flux, total EUV intensity, (bottom) maximum magnetic field, and maximum EUV intensity for NOAA AR 10377. The axes of the plots are split between left (magnetic-field properties, black crosses) and right (coronal properties, blue squares). RHESSI flares associated with the AR are indicated by downward arrows.

In the top panel of Figure 10, the emergence of the magnetic structure of 10377 is clearly seen in measurements of its total flux. The AR is stable until ≈ 8 June 2003 when a phase of rapid emergence begins, lasting until ≈ 11 June when the total magnetic flux has more than doubled. Comparing Figure 9 and Figure 10, we see that the total magnetic flux increases faster than the magnetic area, implying that the AR magnetic fields emerge relatively faster than they diffuse. The same general smooth trend is observed in the SPOCA total EUV intensity between 6 and 11 June. After NOAA 10377 merges with 10375 on 11 June, we see a clear decay of the total EUV intensity in this combined region. Note that both SMART flux and SPOCA total EUV intensity behave similarly to the region area time series.

In the bottom panel the maximum magnetic field is much less stable than the flux, and shows no clear trend. The maximum SPOCA EUV intensity does not change significantly between 6 and 11 June for NOAA region 10377, but exhibits three clear peaks afterwards which can be attributed to region 10375. The first peak, on 11 June, can be attributed to SPOCA merging with NOAA 10375. The peak on 12 June, near 1300, is probably associated with the M1.0 flare in 10375 at around 1358 UT, whereas the 13 June 0700 UT peak is probably related to the M1.8 (0628 UT) or C6.1 (0710 UT) flares in 10375. These flares (appearing in the NOAA events catalogue) are not indicated by the RHESSI arrows, since we have only displayed those flares attributed to 10377. This shows that SPOCA maximum intensity is capable of indicating solar eruptions.

Magnetic properties related to polarity mixing and complexity are shown in Figure 11. In the top panel, the angle between the bipole connection line and

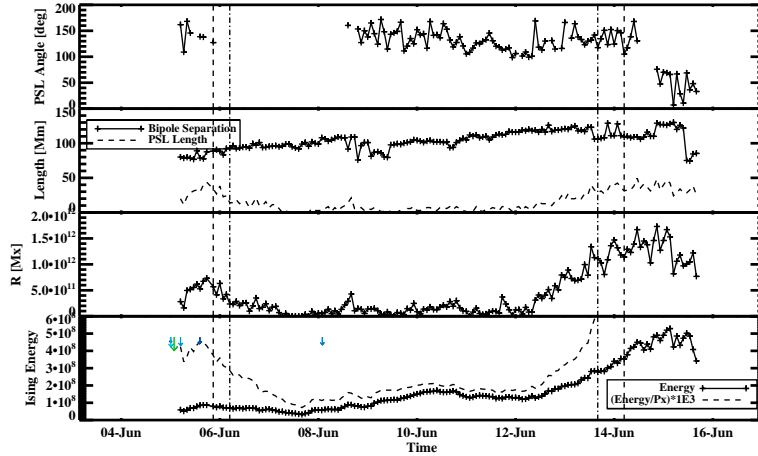


Figure 11. Time series of (top) PSL orientation with respect to the bipole separation line, (middle-top) bipole separation line length (crosses) and PSL length (dashed), (middle-bottom) R , and (bottom) Ising energy (crosses) and Ising energy per pixel (dashed; multiplied by 1000 for display) for NOAA AR 10377.

polarity separation line (PSL) is presented. Since the PSL in this AR is only a few megameters (or pixels) long (*cf.* middle-top panel), this angle cannot be measured in a reliable way. Indeed, a small growth in the PSL detection in any direction can cause the angle to change dramatically. In the middle-bottom panel the total flux near the PSL [R] is very small until it begins to increase as a false PSL is detected due to the near-horizontal fields of the large leading polarity sunspot approaching the west limb on 12 June.

Ising energy, a proxy for magnetic connectivity, is shown in the bottom panel. This property increases during the main magnetic emergence phase (≈ 8 to 10 June 2003) since it is dependent on the magnetic-field strength and inversely dependent on the distance between individual magnetic elements. The Ising energy per pixel (dashed line) appears to be very susceptible to geometrical effects as the large decrease near the west limb and increase near the east limb both coincide with the formation of false PSLs in the leading sunspot. It should be noted that this quantity was calculated without remapping the data to disk-centre as done by Ahmed *et al.* (2010), giving the measurement an even larger viewing-angle dependence.

4.3.2. NOAA 10365

Active region NOAA 10365 rotates onto the visible solar disk on 19 May 2003 at heliographic latitude -5° . At this point 10365 is mature and decaying, having emerged and evolved on the far side of the Sun. On 24 May, a new bipolar structure rapidly emerges in the extended plage of the trailing (positive) polarity. NOAA switches the 10365 designation to this newly emerged bipole several days

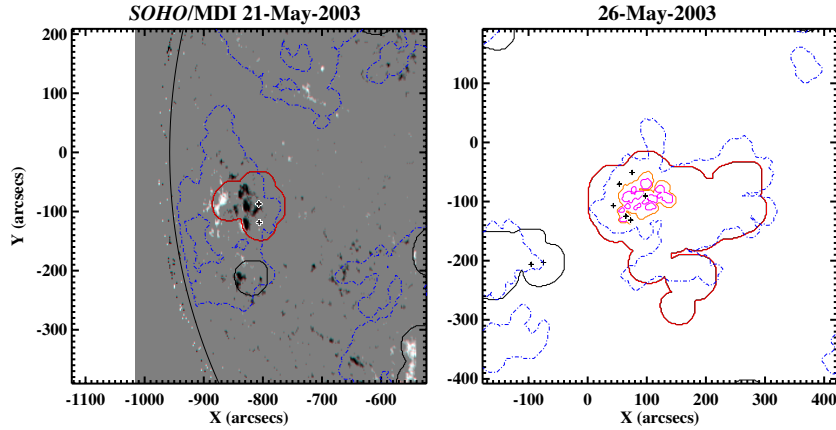


Figure 12. A comparison of detection contours for NOAA AR 10365. ASAP sunspots are represented by black crosses. The contours represent SMART in black (with NOAA 10365 outlined in red) for the magnetic features, SPoCA in dashed blue for coronal features, and STARA in orange for sunspot penumbrae and magenta for umbrae.

later. As the bipole evolves it develops a strong double PSL by merging with the decayed flux. It produces many C- and M-class flares and several X-class flares. The AR progresses around the visible disk, eventually returning as NOAA 10386. The onset of decay occurs as C- and M-class flares are produced with decreasing frequency and the spot areas, magnetic flux, and field strengths decrease.

Figure 12 shows a comparison of the heliographic positions and sizes of two sets of SMART, ASAP, STARA and SPoCA detections of NOAA 10365. We can see that positions of the SMART, ASAP, STARA and SPoCA detections agree well. The SPoCA detection, however, includes coronal loops extending away from the footpoint boundary of NOAA 10365. Before 24 May, SPoCA merges NOAA region 10367 with its detection of 10365. From 24 May–27 May it only detects 10365, on 27 May at 1300 UT there is a single data point where these regions are merged by SPoCA, and from 29 May at 0100 UT onwards, SPoCA merges them for the remaining observation period. The longitudes of all detections within 24–27 May agree well. After 27 May the SPoCA longitude drifts, reflecting changes in the merged coronal structures. Unlike 10377, the magnetic centroid of 10365 at first trails behind the sunspot centroid but then precedes it, as evidenced by the top panel in Figure 13. This is because the new bipole, which develops many spots, emerges behind the existing weakly spotted bipole. The new emergence is clear in the plot of total sunspot area (middle panel), and is unclear in the magnetic and EUV area plots since the new bipole emerges partially within the boundary of the old one. Note that all areas for NOAA 10365 are much larger than those for simpler region 10377. For SMART, area is very sensitive to weak magnetic plage, however. This can be seen in the sudden jumps around May 25 and 28, which are due to nearby plage temporarily merging with the AR. The jump in STARA area on 27 May can be attributed to a bad data file (note that there is no ASAP data point at that time).

From 25 May onwards, the total magnetic flux increases gradually to over four-fold the initial value during development and levels off around 29 May (see

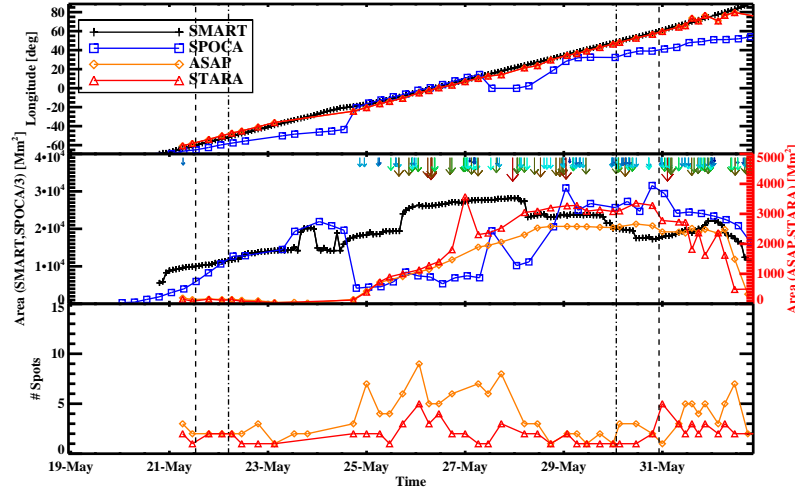


Figure 13. Time series of position, area, and sunspot information characterising the evolution of NOAA AR 10365. The legend indicates symbols and colors for each of the detection algorithms. The axes of the area plot are split between left (SPoCA and SMART) and right (ASAP and STARA). The SPoCA areas have been divided by three for display.

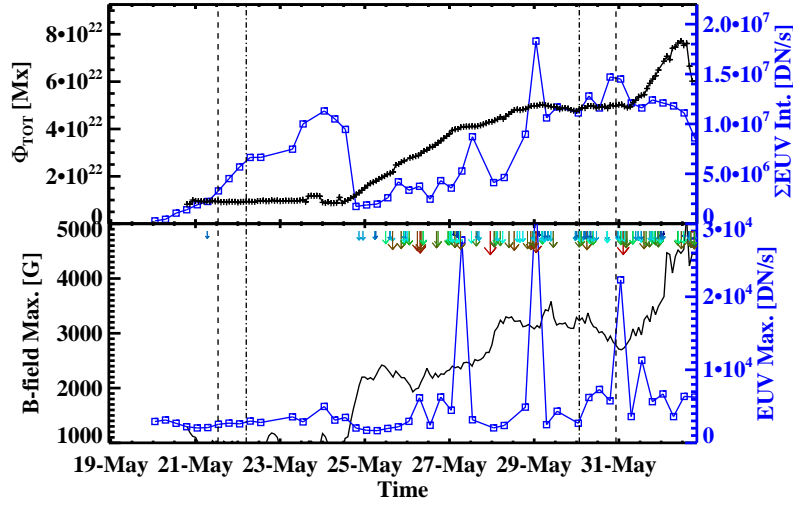


Figure 14. Time series of (top) total magnetic flux, total EUV intensity, (bottom) maximum magnetic field, and maximum EUV intensity for NOAA AR 10365. The axes of the plots are split between left (magnetic-field properties, black crosses) and right (coronal properties, blue squares). RHESSI flares associated with the AR are indicated by downward arrows.

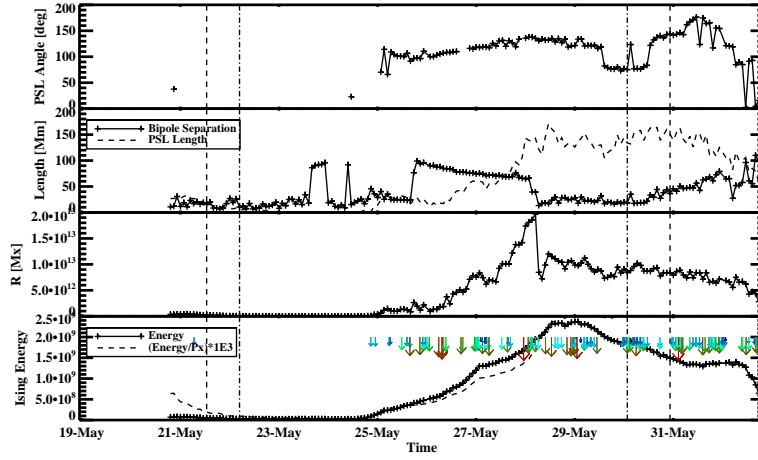


Figure 15. Time series showing proxies for the complexity and polarity mixing in NOAA AR 10365. (middle-top) bipole separation line length (crosses) and PSL length (dashed), (middle-bottom) R , and (bottom) Ising energy (crosses) and Ising energy per pixel (dashed; multiplied by 1000 for display)

Figure 14). The maximum magnetic field increases abruptly on 25 May and also increases over time, albeit less smoothly than the magnetic flux. The maximum magnetic field did not show an overall increasing or decreasing trend in the case of simpler NOAA region 10377.

The time series of SPoCA maximum intensity exhibits some peaks, which can be related to the following flares produced by NOAA 10365: the M1.9 flare at 0534 UT on 26 May, the M1.6 flare at 0506 UT on 27 May, the X1.2 flare at 0051 UT on 29 May, and the M9.3 flare at 0213 UT on 31 May. The last two flares are even visible in the total SPoCA intensity, which shows more or less a gradual increase over time, but less smooth than in the case of the simpler NOAA region 10377. The flares not picked up by SPoCA likely occurred in between EIT images.

Signatures in the evolution of the magnetic topology of NOAA 10365 precede its intense coronal activity, indicated by the associated RHESSI flares in Figure 15. Just before 25 May 2003 the new emergence causes a jump in the main bipole separation line length. As the emergence continues and strong PSLs develop, this length decreases, while the total PSL length increases, as shown in the middle-top panel of Figure 15. Also, there are signs of gradual helicity injection as the angle between the main bipole connection line and the main PSL grows from near perpendicular (90°) to around 120° (top panel). The flux near PSL $[R]$ grows during this time, as does the Ising energy (middle-bottom and bottom panels, respectively). A bump in R just before 26 May is followed by an intense RHESSI flare. Intense flaring begins again around the second bump in R on 28 June. Examining the development of Ising energy, it appears that sharp increases in the property are followed by the most intense flaring.

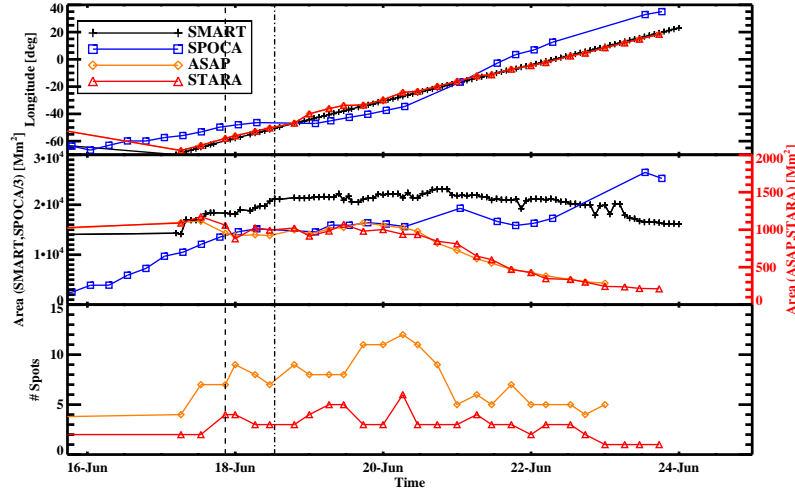


Figure 16. Time series of position, area, and sunspot information characterising the decay phase of NOAA AR 10365 (renamed 10386) during its second disk passage. The legend indicates symbols and colors for each of the detection algorithms. The axes of the area plot are split between left (SPoCA and SMART) and right (ASAP and STARA). The SPoCA areas have been divided by three for display.

NOAA 10365 returns for a second disk passage, renamed 10386. We are able to observe its decay phase, as shown in Figures 16 – 18. As no RHESSI data on flares is available for this period, no flare arrows were added to these figures. While the longitude of the SMART magnetic centroid increases linearly with time, the ASAP and STARA sunspot centroids show small departures from this line between 19 and 21 June, preceding the magnetic centroid. The SPoCA detection of NOAA 10386 merges with 10388 and 10389, so a direct comparison with the other algorithms cannot be made.

The magnetic area does not change significantly, but the total sunspot area clearly decreases (middle panel, Figure 16), and has already decreased substantially since the previous disk passage (as NOAA 10365). The total magnetic flux decreases (top panel, Figure 17) as its magnetic fields diffuse and weaken. Comparing the values to Figure 14, we notice that the flux had already decreased significantly since the previous solar rotation. The total EUV intensity does not change substantially, regardless of the weakening magnetic footpoints, although it has decreased since the previous solar rotation. Its increase on 22 June is due to the detection merging with a large region near the limb. The maximum magnetic-field value shows a gradual, although not very smooth decrease, and has also decreased since the previous passage. The maximum EUV intensity does not show a clear trend, and although several jumps are detected, the intensity levels are much less than those associated with flares over the previous passage. The peak on 18 June at 0100 UT, for instance, can likely be associated to the M6.8 flare produced by region 10386 at 2227 UT on 17 June. The PSL length has

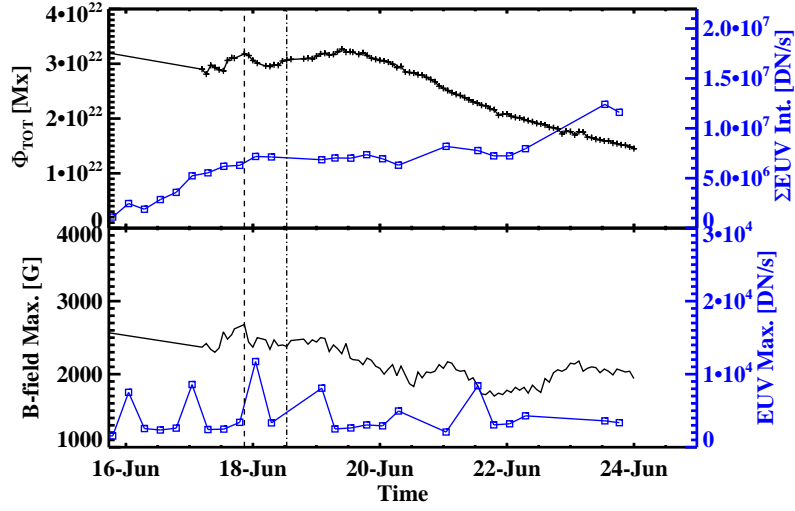


Figure 17. Time series of (top) total magnetic flux, total EUV intensity, (bottom) maximum magnetic field, and maximum EUV intensity for NOAA AR 10365 on its second disk passage as 10386. The axes of the plots are split between left (magnetic-field properties, black crosses) and right (coronal properties, blue squares).

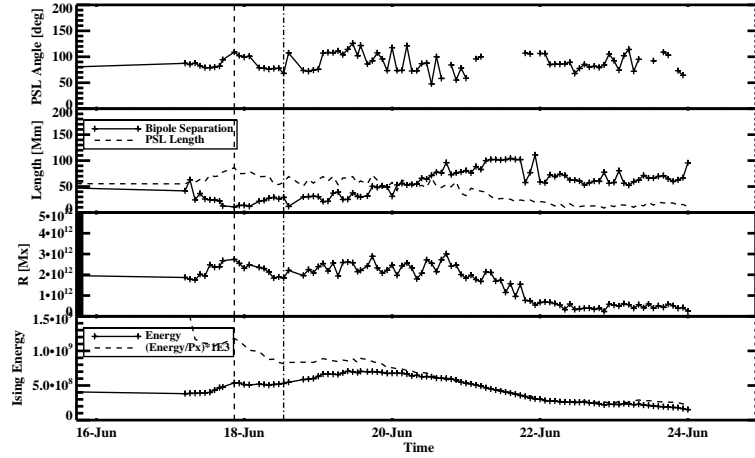


Figure 18. Time series showing proxies for the complexity and polarity mixing in NOAA 10386. (top) PSL orientation with respect to the bipole separation line, (middle-top) bipole separation line length (crosses) and PSL length (dashed), (middle-bottom) R , and (bottom) Ising energy (crosses) and Ising energy per pixel (dashed; multiplied by 1000 for display)

decreased since the previous solar rotation, and shows a further gradual decrease in Figure 18. The same is true for both R and the Ising energy.

5. Discussion and Conclusion

In this article the performance of the presented algorithms is tested in several ways: the overall detection performances are investigated as compared to established methods; the correlations between extracted physical properties are determined using Principal Component Analysis; the stability and usefulness of the algorithms and of various feature properties for studying feature time-evolution is tested. Additionally, some lessons were learned about data analysis using automated detection algorithms. The following relates the main results of these investigations.

In Section 4.1 we compared ASAP, STARA, SIDC, and NOAA sunspot detections and found out that although different numbers of features are detected, the total disk areas agree well. The same is true for the comparison between SMART and SPoCA active-region detections. The difference in numbers can be explained as follows: ASAP is sensitive to pores while STARA only detects developed sunspots. Pores clearly do not add significant area to the total disk coverage, while there is a large number of them detected. NOAA sunspot counts include both penumbrae and umbral cores, whereas ASAP and STARA only count sunspot groups. Consequently, sunspot counts should be very carefully assessed when applied to a long-term inhomogeneous historical record. NOAA only counts those active regions that possess sunspots, which is not the case for SMART nor SPoCA. SMART detects both small AR fragments as well as complexes of bipolar structures, while SPoCA is sensitive to bright loop connections between adjacent features, often merging them into a single detection. These differences are partially dependent on thresholds chosen by the developers and may be tuned to return an agreeable feature boundary. Boundaries are inherently arbitrary as there is no established definition of each feature. Additionally, features evolve continuously and are prone to merging and fragmentation, so universally defining a feature is very difficult. The summed area of features is a preferred quantity as it is both more stable and less ambiguous.

The use of Principal Component Analysis (Section 4.2) has allowed us to determine which feature properties contain the most information about our data set. PCA also tends to separate photospheric and coronal contribution. Features computed at the photospheric level such as R , L_{sg} , Ising energy, ASAP sunspot area, and magnetic flux are highly correlated to each other and have a large contribution to the first component, which accounts for 52.86% of the variability in the total data set. The maximum, variance, skewness, and kurtosis in EUV intensity images are highly correlated to each other and moderately correlated to both the first and second principal components. By reducing dimensionality the accuracy and robustness of a classification scheme can be enhanced (Jiang, 2011). For example, this could be used to discriminate between flaring and non-flaring active regions properties.

Through the time series analysis of two AR case studies (Section 4.3), we have observed three physical processes evident in their evolution: emergence of

a bipolar magnetic structure, sunspots, and EUV loops (Section 4.3.1); increase and peak in non-potentiality, followed by the onset of flaring (Section 4.3.2); decay and weakening of magnetic footpoints (Section 4.3.2). We find that the algorithms show good correspondence between centroid positions and areas but significant divergence is seen in other properties.

In the case study of the simple active region NOAA 10377 (Section 4.3.1) we see that the total number of detected sunspots fluctuates wildly as transient spots rapidly emerge and disappear. This is partly due to the visibility curve since the area of small spots is highly impacted by the observer's viewing angle (Dalla, Fletcher, and Walton, 2008; Watson *et al.*, 2009). In order to study AR evolution, sunspot area is more indicative of the emergence and decay of an AR than coronal or magnetic area, which do not necessarily decrease during decay (see Section 4.3). As a basis for long-term AR tracking, magnetic flux is more useful than the sunspot area (since sunspots are much more transient than their magnetic footprints) or maximum magnetic field value (since it is affected by the MDI saturation problem Liu, Norton, and Scherrer (2007)). Also, the maximum magnetic-field value is unstable since different positions in the active region will over-take each other in field magnitude as they develop, causing the location that the value is sampled from to vary wildly. Finally, the total EUV intensity determined by SPoCA has a smooth behaviour over time and is closely linked to area. The maximum EUV intensity peaks when the active region emits a large flare, and appears to be a useful indicator of eruptions in the corona.

The case study of complex, flaring NOAA 10365 (Section 4.3.2) shows that flaring can happen both in periods of flux emergence as well as non-potentiality enhancement in an active region. Following the initial flaring during the emergence phase of evolution, further flaring occurs as the main PSL rotates with respect to the bipole connection line. This is a sign of helicity injection and is coincident with increases of other properties related to polarity mixing. Helicity injection has been established as a method of increasing non-potentiality and may be caused by the emergence of subsurface twisted flux ropes, as seen in Dun *et al.* (2007).

As NOAA 10365 returns after one solar rotation, decay is seen in the strength of its magnetic footprint. However, the area is not seen to decrease significantly, since supergranular diffusion causes a radial dispersal of magnetic elements. Coronal structures do not appear to decay readily, either. This result agrees with Lites *et al.* (1995), where it is reasoned that if the coronal magnetic structure is closed, it may be in a state of quasi-static equilibrium, whereby the magnetic buoyancy of the loops is cancelled by the weight of plasma trapped at the bottom of the closed structure.

By performing these studies, it is found that magnetic active-region detections provide the most stable base for feature tracking. Sunspots are only visible for short periods of time, and coronal detections continually form bright loop connections to nearby features. The simple feature tracking method used in this article (see Section 3.5) is novel in that it allows features to be tracked between multiple disk passages. This is essential for analysing the complete life-cycle of an active region, as exemplified in the analysis of NOAA 10365 (Section 4.3.2). Future work on active-region evolution should combine morphological information to better

handle merging and splitting (as done by Welsch and Longcope (2003)) with our method of multiple disk passage tracking. Future work on our algorithms will also address the automatic detection and handling of structural or visible errors in solar data, to avoid discontinuities in the time series due to a corrupted image, as was seen in the STARA outputs used in the case studies (see Section 4.3.1).

This work will be expanded in the future to include an analysis of the full SOHO archive as well as detailed studies of photospheric and coronal SDO data sets. Many physical studies will benefit from this work, as investigations that examine coronal heating as a result of large scale magnetic fields (Schrijver, 1987; Fisher *et al.*, 1998), coupling between the photosphere and corona (Handy and Schrijver, 2001), sources of coronal mass ejections (Subramanian and Dere, 2001), flux emergence and distribution (Liu and Kurokawa, 2004; Abramenko and Longcope, 2005) and flare forecasting (Gallagher, Moon, and Wang, 2002) can all be repeated with these automated detection methods. Using these methods allows a far greater number of features to be analysed and reduces human bias in the detection of features in the solar data.

The algorithms presented here are automated (once thresholds have been fixed), independent, and unsupervised. Although some development remains to be done, they detect features the way that they are intended, and will provide useful additions to the SDO pipeline feature-detection methods. However, this work shows that automated methods cannot replace human data analysis but they can help to stream-line the process.

Acknowledgements Funding of CV and VD by the Belgian Federal Science Policy Office (BELSPO) through the ESA/PRODEX SIDC Data Exploitation program, as well as by the Solar–Terrestrial Center of Excellence/ROB, is hereby appreciatively acknowledged. FTW acknowledges Ph. D. funding from the Science and Technology Facilities Council and the guidance of his supervisor, Lyndsay Fletcher. We acknowledge support from ISSI through funding for the International Team on “Mining and exploiting SDO data in Europe” led by V. Delouille. ASAP is supported by an EPSRC Grant (EP/F022948/1), which is entitled “Image Processing, Machine Learning and Geometric Modelling for the 3D Representation of Solar Features”. PAH acknowledges support from ESA/PRODEX and a grant from the EC Framework Programme 7 (HELIO) and the guidance of his supervisor, Peter T. Gallagher. We would like to thank the SOHO team for making both their data and analysis software publicly available, Omar W. Ahmed for use of the Ising Energy software, and Aidan M. O’Flanagan for advice on the RHESSI flare list.

References

- Abramenko, V.I., Longcope, D.W.: 2005, Distribution of the Magnetic Flux in Elements of the Magnetic Field in Active Regions. *Astrophys. J.* **619**, 1160–1166. doi:10.1086/426710.
- Ahmed, O., Qahwaji, R., Colak, T., DudokDeWit, T., Ipson, S.: 2010, A new technique for the calculation and 3d visualisation of magnetic complexities on solar satellite images. *The Visual Computer* **26**, 385–395. 10.1007/s00371-010-0418-1. <http://dx.doi.org/10.1007/s00371-010-0418-1>.

- Aschwanden, M.J.: 2010, Image Processing Techniques and Feature Recognition in Solar Physics. *Solar Phys.* **262**, 235–275. doi:10.1007/s11207-009-9474-y.
- Barra, V., Delouille, V., Kretzschmar, M., Hochedez, J.: 2009, Fast and robust segmentation of solar EUV images: algorithm and results for solar cycle 23. *Astron. Astrophys.* **505**, 361–371. doi:10.1051/0004-6361/200811416.
- Benkhalil, A., Zharkova, V.V., Zharkov, S., Ipson, S.: 2006, Active Region Detection and Verification With the Solar Feature Catalogue. *Solar Phys.* **235**, 87–106. doi:10.1007/s11207-006-0023-7.
- Bentley, R.D., Aboudarham, J., Csillaghy, A., Jacquey, C., Hapgood, M.A., Messerotti, M., Gallagher, P., Bocchialini, K., Hurlburt, N.E., Roberts, D., Sanchez Duarte, L.: 2009, Addressing Science Use Cases with HELIO. *AGU Fall Meeting Abstracts*, A6.
- Colak, T., Qahwaji, R.: 2008, Automated McIntosh-Based Classification of Sunspot Groups Using MDI Images. *Solar Phys.* **248**, 277–296. doi:10.1007/s11207-007-9094-3.
- Colak, T., Qahwaji, R.: 2009, Automated Solar Activity Prediction: A hybrid computer platform using machine learning and solar imaging for automated prediction of solar flares. *Space Weather* **7**, S06001. doi:10.1029/2008SW000401.
- Colak, T., Ahmed, O.W., Qahwaji, R., Higgins, P.A.: 2010, Automated Solar Flare Prediction: Is it a Myth? *Presentation in Seventh European Space Weather Week*. <http://spaceweather.inf.brad.ac.uk/colak19nov.pdf>.
- Colak, T., Qahwaji, R., Ipson, S., Ugail, H.: 2011, Representation of Solar Features in 3D for Creating Visual Solar Catalogues. *Adv. Space Res.* **47**(12), 2092–2104. doi:10.1016/j.asr.2010.08.030.
- Conlon, P.A., Gallagher, P.T., McAteer, R.T.J., Ireland, J., Young, C.A., Kestener, P., Hewett, R.J., Maguire, K.: 2008, Multifractal Properties of Evolving Active Regions. *Solar Phys.* **248**, 297–309. doi:10.1007/s11207-007-9074-7.
- Conlon, P.A., McAteer, R.T.J., Gallagher, P.T., Fennell, L.: 2010, Quantifying the Evolving Magnetic Structure of Active Regions. *Astrophys. J.* **722**, 577–585. doi:10.1088/0004-637X/722/1/577.
- Curto, J.J., Blanca, M., Martínez, E.: 2008, Automatic Sunspots Detection on Full-Disk Solar Images using Mathematical Morphology. *Solar Phys.* **250**, 411–429. doi:10.1007/s11207-008-9224-6.
- Dalla, S., Fletcher, L., Walton, N.A.: 2008, Invisible sunspots and rate of solar magnetic flux emergence. *Astron. Astrophys.* **479**, 1–4. doi:10.1051/0004-6361:20078800.

- DeForest, C.E., Hagenaar, H.J., Lamb, D.A., Parnell, C.E., Welsch, B.T.: 2007, Solar Magnetic Tracking. I. Software Comparison and Recommended Practices. *Astrophys. J.* **666**, 576–587. doi:10.1086/518994.
- Delaboudinière, J., Artzner, G.E., Brunaud, J., Gabriel, A.H., Hochedez, J.F., Millier, F., Song, X.Y., Au, B., Dere, K.P., Howard, R.A., Kreplin, R., Michels, D.J., Moses, J.D., Defise, J.M., Jamar, C., Rochus, P., Chauvineau, J.P., Marioge, J.P., Catura, R.C., Lemen, J.R., Shing, L., Stern, R.A., Gurman, J.B., Neupert, W.M., Maucherat, A., Clette, F., Cugnon, P., van Dessel, E.L.: 1995, EIT: Extreme-Ultraviolet Imaging Telescope for the SOHO Mission. *Solar Phys.* **162**, 291–312. doi:10.1007/BF00733432.
- Dougherty, E.R., Lotufo, R.A.: 2003, *Hands-on morphological image processing*, SPIE Optical Engineering Press, Washington, 130.
- Dudok de Wit, T., Auchère, F.: 2007, Multispectral analysis of solar EUV images: linking temperature to morphology. *Astron. Astrophys.* **466**, 347–355. doi:10.1051/0004-6361:20066764.
- Dudok de Wit, T.D.: 2006, Fast Segmentation of Solar Extreme Ultraviolet Images. *Solar Physics* **239**, 519–530.
- Dun, J., Kurokawa, H., Ishii, T.T., Liu, Y., Zhang, H.: 2007, Evolution of Magnetic Nonpotentiality in NOAA AR 10486. *Astrophys. J.* **657**, 577–591. doi:10.1086/510373.
- Falconer, D.A., Moore, R.L., Gary, G.A.: 2008, Magnetogram Measures of Total Nonpotentiality for Prediction of Solar Coronal Mass Ejections from Active Regions of Any Degree of Magnetic Complexity. *Astrophys. J.* **689**, 1433–1442. doi:10.1086/591045.
- Fisher, G.H., Longcope, D.W., Metcalf, T.R., Pevtsov, A.A.: 1998, Coronal Heating in Active Regions as a Function of Global Magnetic Variables. *Astrophys. J.* **508**, 885–898. doi:10.1086/306435.
- Gallagher, P.T., Moon, Y., Wang, H.: 2002, Active-Region Monitoring and Flare Forecasting I. Data Processing and First Results. *Solar Phys.* **209**, 171–183. doi:10.1023/A:1020950221179.
- Georgoulis, M.K., Rust, D.M.: 2007, Quantitative Forecasting of Major Solar Flares. *Astrophys. J. Lett.* **661**, 109–112. doi:10.1086/518718.
- Habash Krause, L., Franz, A., Stevenson, A.: 2011, On the application of Exploratory Data Analysis for characterization of space weather data sets. *Adv. Space Res.* **47**, 2199–2209. doi:10.1016/j.asr.2011.03.017.
- Handy, B.N., Schrijver, C.J.: 2001, On the Evolution of the Solar Photospheric and Coronal Magnetic Field. *Astrophys. J.* **547**, 1100–1108. doi:10.1086/318429.

- Hewett, R.J., Gallagher, P.T., McAteer, R.T.J., Young, C.A., Ireland, J., Conlon, P.A., Maguire, K.: 2008, Multiscale Analysis of Active Region Evolution. *Solar Phys.* **248**, 311–322. doi:10.1007/s11207-007-9028-0.
- Higgins, P.A., Gallagher, P.T., McAteer, R.T.J., Bloomfield, D.S.: 2011, Solar magnetic feature detection and tracking for space weather monitoring. *Adv. Space Res.* **47**, 2105–2117. doi:10.1016/j.asr.2010.06.024.
- Howard, R.F., Harvey, J.W., Forgach, S.: 1990, Solar surface velocity fields determined from small magnetic features. *Solar Phys.* **130**, 295–311. doi:10.1007/BF00156795.
- Hurlburt, N., Cheung, M., Schrijver, C., Chang, L., Freeland, S., Green, S., Heck, C., Jaffey, A., Kobashi, A., Schiff, D., Serafin, J., Seguin, R., Slater, G., Somani, A., Timmons, R.: 2010, Heliophysics Event Knowledge-base for the Solar Dynamics Observatory (SDO) and Beyond. *Solar Phys.* doi:10.1007/s11207-010-9624-2.
- Jiang, X.: 2011, Linear subspace learning-based dimensionality reduction. *IEEE Signal Processing Magazine* **28**(2), 16–26.
- Jolliffe, I.T.: 2002, *Principal component analysis, 2nd edition*, Springer, New York, 487 p.
- Krishnapuram, R., Keller, J.M.: 1993, A possibilistic approach to clustering. *IEEE Transactions on Fuzzy Systems* **1**, 98–110.
- Krishnapuram, R., Keller, J.M.: 1996, The Possibilistic C-Means Algorithm: Insights and Recommendations. *IEEE Transactions on Fuzzy Systems* **4**, 385–393.
- LaBonte, B.J., Georgoulis, M.K., Rust, D.M.: 2007a, Survey of Magnetic Helicity Injection in Regions Producing X-Class Flares. *Astrophys. J.* **671**, 955–963. doi:10.1086/522682.
- LaBonte, B.J., Georgoulis, M.K., Rust, D.M.: 2007b, Survey of Magnetic Helicity Injection in Regions Producing X-Class Flares. *Astrophys. J.* **671**, 955–963. doi:10.1086/522682.
- Lefebvre, S., Rozelot, J.: 2004, A new method to detect active features at the solar limb. *Solar Phys.* **219**, 25–37. doi:10.1023/B:SOLA.0000021818.97402.1e.
- Leka, K.D., Barnes, G.: 2007, Photospheric Magnetic Field Properties of Flaring versus Flare-quiet Active Regions. IV. A Statistically Significant Sample. *Astrophys. J.* **656**, 1173–1186. doi:10.1086/510282.
- Lites, B.W., Low, B.C., Martinez Pillet, V., Seagraves, P., Skumanich, A., Frank, Z.A., Shine, R.A., Tsuneta, S.: 1995, The Possible Ascent of a Closed Magnetic System through the Photosphere. *Astrophys. J.* **446**, 877–. doi:10.1086/175845.

- Liu, Y., Kurokawa, H.: 2004, On a Surge: Properties of an Emerging Flux Region. *Astrophys. J.* **610**, 1136–1147. doi:10.1086/421715.
- Liu, Y., Norton, A.A., Scherrer, P.H.: 2007, A Note on Saturation Seen in the MDI/SOHO Magnetograms. *Solar Phys.* **241**, 185–193. doi:10.1007/s11207-007-0296-5.
- Martens, P.C.H., Attrill, G.D.R., Davey, A.R., Engell, A., Farid, S., Grigis, P.C., Kasper, J., Korreck, K., Saar, S.H., Savcheva, A., Su, Y., Testa, P., Wills-Davey, M., Bernasconi, P.N., Raouafi, N., Delouille, V.A., Hochedez, J.F., Cirtain, J.W., Deforest, C.E., Angryk, R.A., de Moortel, I., Wiegelmann, T., Georgoulis, M.K., McAteer, R.T.J., Timmons, R.P.: 2011, Computer Vision for the Solar Dynamics Observatory (SDO). *Solar Phys.* doi:10.1007/s11207-010-9697-y.
- McAteer, R.T.J., Gallagher, P.T., Ireland, J., Young, C.A.: 2005, Automated Boundary-extraction And Region-growing Techniques Applied To Solar Magnetograms. *Solar Phys.* **228**, 55–66. doi:10.1007/s11207-005-4075-x.
- Morita, S., McIntosh, S.W.: 2005, Genesis of AR NOAA10314. In: K. Sankarasubramanian, M. Penn, & A. Pevtsov (ed.) *Large-scale Structures and their Role in Solar Activity* **346**, Astron. Soc. Pacific, San Francisco, 317–.
- Nguyen, S.H., Nguyen, T.T., Nguyen, H.S.: 2005, Rough set approach to sunspot classification problem. In: Slezak, D., Yao, J., Peters, J.F., Ziarko, W., Hu, X. (eds.) *Rough Sets, Fuzzy Sets, Data Mining, and Granular Computing Lecture Notes in Computer Science* **3642**, Springer, Berlin / Heidelberg, 263–272.
- Parnell, C.E., DeForest, C.E., Hagenaar, H.J., Johnston, B.A., Lamb, D.A., Welsch, B.T.: 2009, A Power-Law Distribution of Solar Magnetic Fields Over More Than Five Decades in Flux. *Astrophys. J.* **698**, 75–82. doi:10.1088/0004-637X/698/1/75.
- Pérez-Suárez, D., Higgins, P.A., McAteer, R.T.J., Bloomfield, D.S., Gallagher, P.T.: 2011, Automated Solar Feature Detection for Space Weather Applications. In: Qahwaji, R., Green, R., Hines, E.L. (eds.) *Applied Signal and Image Processing: Multidisciplinary Advancements*, IGI Global, Hershey, Pennsylvania, 207–225. doi:10.4018/978-1-60960-477-6.
- Qahwaji, R., Colak, T.: 2006, Hybrid imaging and neural networks techniques for processing solar images. *I. J. Comput. Appl.* **13**(1), 9–16.
- Sarro, L.M., Berihuete, A.: 2011, Statistical techniques for the detection and analysis of solar explosive events. *Astron. Astrophys.* **528**, A62+. doi:10.1051/0004-6361/201014894.
- Scherrer, P.H., Bogart, R.S., Bush, R.I., Hoeksema, J.T., Kosovichev, A.G., Schou, J., Rosenberg, W., Springer, L., Tarbell, T.D., Title, A., Wolfson, C.J., Zayer, I., MDI Engineering Team: 1995, The Solar Oscillations Investigation - Michelson Doppler Imager. *Solar Phys.* **162**, 129–188. doi:10.1007/BF00733429.

- Schrijver, C.J.: 1987, Solar active regions - Radiative intensities and large-scale parameters of the magnetic field. *Astron. Astrophys.* **180**, 241–252.
- Schrijver, C.J.: 2007, A Characteristic Magnetic Field Pattern Associated with All Major Solar Flares and Its Use in Flare Forecasting. *Astrophys. J. Lett.* **655**, 117–120. doi:10.1086/511857.
- SIDC-Team: 2003, The International Sunspot Number. *Monthly Report on the International Sunspot Number*, online catalogue. <http://www.sidc.be/sunspot-data/dailyssn.php>).
- Subramanian, P., Dere, K.P.: 2001, Source Regions of Coronal Mass Ejections. *Astrophys. J.* **561**, 372–395. doi:10.1086/323213.
- Watson, F., Fletcher, L., Dalla, S., Marshall, S.: 2009, Modelling the Longitudinal Asymmetry in Sunspot Emergence: The Role of the Wilson Depression. *Solar Phys.* **260**, 5–19. doi:10.1007/s11207-009-9420-z.
- Welsch, B.T., Longcope, D.W.: 2003, Magnetic Helicity Injection by Horizontal Flows in the Quiet Sun. I. Mutual-Helicity Flux. *Astrophys. J.* **588**, 620–629. doi:10.1086/368408.
- Zharkov, S., Zharkova, V., Ipson, S., Benkhalil, A.: 2004, Automated recognition of sunspots on the soho/mdi white light solar images. In: *Knowledge-Based Intelligent Information and Engineering Systems Lecture Notes in Computer Science* **3215**, Springer, Berlin / Heidelberg, 446–452.

